Construction and Verification of the Constitutive Model of Pure Copper Deformation at Elevated Temperatures

S. H. Huang,[a,b,1] Y. Wu,[a] Z. D. Zhao,[a,b] and X. S. Xia[a]

[a] Southwest Technology and Engineering Research Institute, Chongqing, China

[b] Precision Forming Integrated Manufacturing Technology of Collaborative Innovation Center, Chongqing, China

[1] hsh82@163.com

The deformation behavior of pure copper was studied in hot compression tests in the temperature range of 773–1173 K and strain rate interval of 0.001–1.0 s^{-1}, the corresponding flow stress curves were plotted. The new method to calculate critical and saturation stresses was devised, quantitative analysis of strain hardening and dynamic softening was presented, a three-stage constitutive model was constructed to predict the flow stress of pure copper. As predicted and measured flow stress comparison indicate, the physical constitutive model can accurately characterize hot deformation of pure copper. With dynamic recovery and/or recrystallization. Numerical simulation of an upsetting process is carried out by implementing the constitutive model into commercial software. This model can be put to practical use and be quite promising for improving efficiency of a hot forging process for pure copper components.

Keywords: pure copper, constitutive model, flow stress, numerical simulation, dynamic recrystallization.

N o t a t i o n

DRV	–	dynamic recovery
DRX	–	dynamic recrystallization
X_{drx}	–	DRX fraction
σ, ε	–	stress and strain, respectively
σ_{wh}	–	work hardening stress
σ_{rec}	–	dynamic recovery stress
σ_{reci}	–	ith process stress
σ_{drx}	–	dynamic recrystallization stress
σ_{sat}	–	saturated stress
σ_0, ε_0	–	initial yield stress and strain
σ_c, ε_c	–	critical stress and strain
σ_p, ε_p	–	peak stress and strain
$\sigma_{ss}, \varepsilon_{ss}$	–	steady state stress and strain
ε_i	–	ith process strain
r	–	parameter of DRV
n, k	–	Avrami's power and constant
T	–	temperature
T_r	–	reference temperature
T_m	–	melting point of the material

σ_{0r}	–	yield stress at reference temperature and particular strain rate
θ	–	strain hardening rate
θ'_c	–	primary partial derivative value of θ and σ corresponding to critical stress σ_c
$\theta''_{T,\dot{\varepsilon}}$	–	secondary partial derivative function of strain hardening rate vs stress
$\dot{\varepsilon}$	–	strain rate
$\dot{\varepsilon}_r$	–	reference strain rate
B, C, q	–	constants of Johnson–Cook model
a_i, b_j, c_k	–	parameters ($i = 0, 1, ..., 9$; $j = 0, 1, ..., 5$; $k = 0, 1, ..., 3$)

Introduction. Pure copper, with its excellent combination of such properties as good plasticity and high density, is widely applied to the manufacturing of high-precision and complex products [1, 2]. To achieve the process optimization and obtain products with precise geometrical shape and fine and uniform crystalline grains, it is required to study the high-temperature deformation behavior of pure copper. Thermal simulation compression test is often used to simulate condition of forging technology, and a constitutive model of the material is established to reveal the work hardening and softening behaviors and provide a numerical simulation of the products' processing [3–5].

It is well known that the main softening mechanisms of alloys under hot deformation are dynamic recovery (DRV) and dynamic recrystallization (DRX) [6–13]. The flow stress functions of DRV and DRX are given by Eqs. (1) and (2), respectively:

$$\sigma_{rec} = \{\sigma_{sat}^2 - (\sigma_{sat}^2 - \sigma_0^2)\exp[-r(\varepsilon - \varepsilon_0)]\}^{1/2}, \qquad \varepsilon_0 \leq \varepsilon \leq \varepsilon_c, \tag{1}$$

$$\sigma_{drx} = \sigma_{rec} - (\sigma_{sat} - \sigma_{ss})\left\{1 - \exp\left[-k\left(\frac{\varepsilon - \varepsilon_c}{\varepsilon_p}\right)^n\right]\right\}, \qquad \varepsilon_c \leq \varepsilon \leq \varepsilon_{ss}. \tag{2}$$

If the DRX does not initiate, as shown in Fig. 1a, the so-called saturation stress (if DRV is the only softening mechanism) can be measured directly from the flow curves. If the flow curve displays an apparent softening regime due to DRX, the saturation stress does not practically exist, but nevertheless can be extrapolated from the work-hardening rate curve under the assumption that only DRV occurred (Fig. 1b). The softening caused by DRX can be measured subsequently by using this hypothetical saturation stress and the practical flow curve.
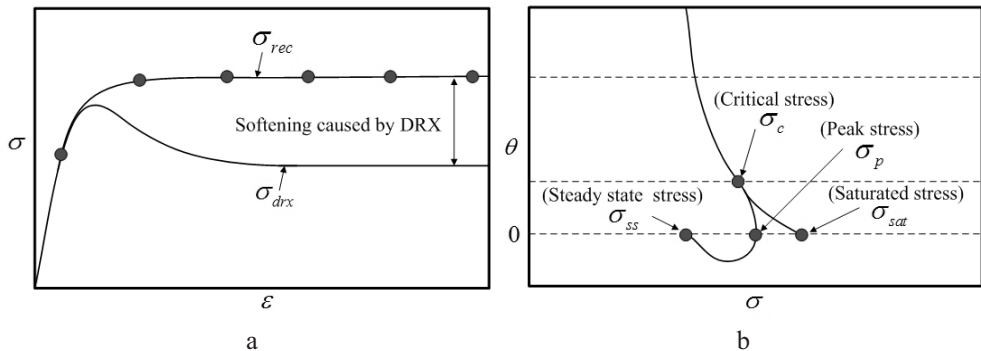

Fig. 1. (a) Schematic description of the flow behavior at high temperature; (b) corresponding flow stress dependence of the strain hardening rate.

At present, the following two methods based on Eq. (1) are mainly used to determine the value of σ_{sat} [6–13]. In the first method, using Eqs. (3) and (4), the linear regression of $\theta\sigma_{rec} - \sigma_{rec}^2$ curve is performed to get m and r values:

$$\theta\sigma_{rec} = \frac{r}{2}(\sigma_{sat}^2 - \sigma_{rec}^2), \qquad \varepsilon_0 \leq \varepsilon \leq \varepsilon_c, \tag{3}$$

$$m = \frac{\partial(\theta\sigma_{rec})}{\partial(\sigma_{rec}^2)} = -\frac{r}{2}, \tag{4}$$

With $\theta\sigma_{rec} = 0$, the stress corresponding to $\theta\sigma_{rec} - \sigma_{rec}^2$ curve is the squared saturation stress σ_{sat}^2.

The second method adopts Eq. (5) to yield the primary partial derivative value θ'_c of θ and σ corresponding to critical stress (σ_c) point. Here the $\theta - \sigma$ curve extends outward to $\theta = 0$ along the tangent line at the critical stress (σ_c) point, and Eq. (6) is used to obtain the saturation stress(σ_{sat}):

$$\theta'_c = \frac{\partial\theta}{\partial\sigma}\bigg|_{\sigma_c}, \tag{5}$$

$$\sigma_{sat} = \sigma_c - \theta_c/\theta'_c. \tag{6}$$

Because of a relatively large fluctuation of the measured stress–strain curve data, there is also a comparatively large scatter in the values of strain hardening rate θ obtained from calculation of $\Delta\sigma/\Delta\varepsilon$. There is no obvious pattern in the $\theta - \sigma$ data curve, as in Fig. 1b, but a relatively large scatter in data exists [4, 5, 12, 13]. It is very difficult to calculate and determine the critical stress σ_c via the above methods, which complicates further determination of such parameters as the saturation stress σ_{sat} and DRV parameter r. Eventually, it deteriorates the accuracy of fitting calculation of Eqs. (1) and (2). In this study, a new method for estimating the critical and saturated stresses is proposed and verified.

1. **Experimental Procedures**. Before the experiment, a pure copper bar was provided by the Luoyang Copper Co., Ltd. (China), which was annealed at 693 K for 2 h, and then scalped to diameter of 8 mm and height of 12 mm from the same area, with grooves on both sides filled with machine oil mingled with graphite powder as lubrication. Then, isothermal compression tests were performed on a Gleeble 1500 thermal-mechanical simulator. The specimens were resistance heated at a heating rate of 1 K/s and held at a certain temperature for 180 s to ensure a uniform starting temperature and decrease the material anisotropy. All specimens were compressed to a true strain of 0.9163 (height reduction of 60%) at the temperatures of 773, 873, 973, 1023, 1073, 1123, and 1173 K, and the strain rates of 0.001, 0.01, 0.1, and 1 s^{-1}. The true compressive stress–strain curves at seven temperatures and four strain rates are shown in Fig. 2.

2. **Principles of Physically-Based Constitutive Model**. Following methods were primarily used to establish constitutive model of pure copper that considers the work hardening and softening effect.

(1) The stress–strain relationship under isothermal constant strain rate was established. To be unified with the function expression in Eq. (1), the function relationship in Eq. (7) was used to conduct fitting calculation of the practically-measured stress–strain data, thereby determining relative parameters of $f(\varepsilon)$ function. Where, $g(\varepsilon)$ is the function related to strain ε. The expressions of primary partial derivative function $f'(\varepsilon)$, secondary
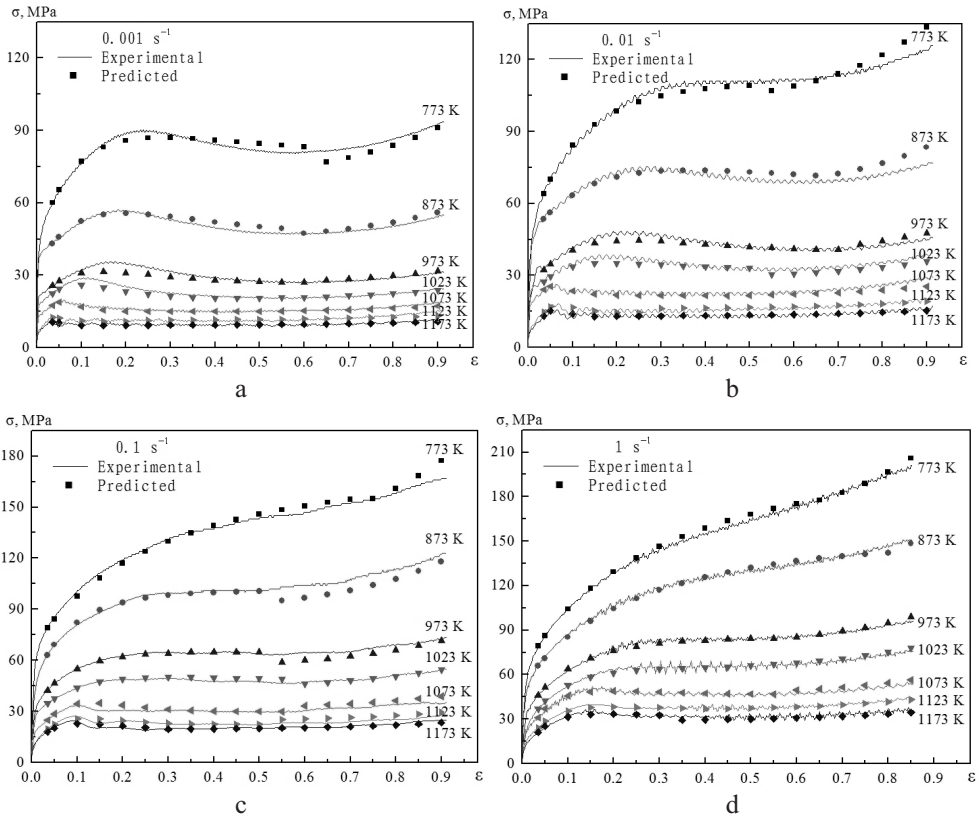
Fig. 2. True stress–strain curves of pure copper at different strain rates: 0.001 (a), 0.01 (b), 0.1 (c), and 1 s^{-1} (d).

partial derivative function $f''(\varepsilon)$, and third partial derivative function $f'''(\varepsilon)$ corresponding to $f(\varepsilon)$ are shown in Eqs. (8), (9), and (10):

$$\ln \sigma_{T,\dot{\varepsilon}} = f(\varepsilon) = \frac{1}{2}\ln\{\sigma_{sat}^2 - (\sigma_{sat}^2 - \sigma_0^2)\exp[g(\varepsilon)]\}, \qquad \varepsilon_0 \le \varepsilon \le 0.9163, \tag{7}$$

$$f'(\varepsilon) = \frac{(\sigma_0^2 - \sigma_{sat}^2)}{2}\exp[g(\varepsilon) - 2f(\varepsilon)]g'(\varepsilon), \tag{8}$$

$$f''(\varepsilon) = \frac{(\sigma_0^2 - \sigma_{sat}^2)}{2}\exp[g(\varepsilon) - 2f(\varepsilon)]\{g''(\varepsilon) + g'(\varepsilon)[g'(\varepsilon) - 2f'(\varepsilon)]\}, \tag{9}$$

$$f'''(\varepsilon) = \frac{(\sigma_0^2 - \sigma_{sat}^2)}{2}\exp[g(\varepsilon) - 2f(\varepsilon)]\begin{Bmatrix} g'''(\varepsilon) \\ +2g''(\varepsilon)[g'(\varepsilon) - 2f'(\varepsilon)] \\ +g'(\varepsilon)[g''(\varepsilon) - 2f''(\varepsilon)] \\ +g'(\varepsilon)[g'(\varepsilon) - 2f'(\varepsilon)]^2 \end{Bmatrix}. \tag{10}$$

The function of strain hardening rate and strain can be derived in the following form:

$$\theta_{T,\dot{\varepsilon}} = \frac{\partial \sigma}{\partial \varepsilon} = \sigma \frac{\partial \ln \sigma}{\partial \varepsilon} = \sigma f'(\varepsilon), \qquad \varepsilon_0 \le \varepsilon \le 0.9163. \tag{11}$$

Established curve of strain hardening rate and stress, or curve of strain hardening rate and strain, when $\theta_{T,\dot{\varepsilon}}$ value was equal to 0 for the first time, peak stress σ_p or peak strain ε_p was determined, and when $\theta_{T,\dot{\varepsilon}}$ was equal to 0 for the second time, steady state stress σ_{ss} or steady state strain ε_{ss} was determined.

(2) Based on Eq. (11) it was deduced to obtain the secondary partial derivative function of strain hardening rate vs stress, as shown in Eq. (12):

$$\theta_{T,\dot{\varepsilon}}'' = \frac{\partial^2 \theta}{\partial \sigma^2} = \frac{f''(\varepsilon) - \dfrac{\{f''(\varepsilon)\}^2}{\{f'(\varepsilon)\}^2} + \dfrac{f'''(\varepsilon)}{f'(\varepsilon)}}{\exp(f(\varepsilon)) f'(\varepsilon)}, \qquad \varepsilon_0 \le \varepsilon \le 0.9163. \tag{12}$$

Under condition of $\varepsilon_0 \le \varepsilon \le \varepsilon_p$, the strain corresponding to the routine calculation objective function $\theta_{T,\dot{\varepsilon}}'' = 0$, i.e., critical strain ε_c, was derived. Thus, the critical stress σ_c was converted from Eq. (7).

(3) Under the condition of $\varepsilon_0 \le \varepsilon_i \le \varepsilon_c$, $\sigma_p \le \sigma_{sat}$, $r > 0$, yield stress σ_0, yield strain ε_0, critical stress σ_c, and critical strain ε_c were substituted into Eqs. (3)–(6) to construct the routine calculation objective function $\sigma_{reci} = \{\sigma_{sat}^2 - (\sigma_{sat}^2 - \sigma_0^2) \exp[g(\varepsilon_i)]\}^{1/2}$ and $\sigma_{sat} = \sigma_c - \theta_c / \theta_c'$, then, $g(\varepsilon_i) = -r(\varepsilon_i - \varepsilon_0)$, where ε_i denotes the ith process strain, σ_{reci} represents ith process stress, calculation was conducted to obtain saturation stress σ_{sat}, parameter r, to get σ_{rec} curve data under isothermal constant strain rate. By repeating the above procedure, σ_{rec} curve data could be obtained under different temperatures and strain rates.

(4) After σ_{rec}, σ_{sat}, σ_{ss}, ε_c, and ε_p data were obtained for different temperatures and strain rates, the measured values σ_{drx} and their corresponding ε data were substituted into Eqs. (13) and (14) [7, 9, 10] to conduct the fitting calculation and obtain n and k values, thereby obtaining σ_{drx} curve data under different temperatures and strain rates:

$$X_{drx} = \frac{\sigma_{rec} - \sigma_{drx}}{\sigma_{sat} - \sigma_{ss}} = \left\{ 1 - \exp\left[-k\left(\frac{\varepsilon - \varepsilon_c}{\varepsilon_p} \right)^n \right] \right\}, \qquad \varepsilon_c \le \varepsilon \le \varepsilon_{ss}, \tag{13}$$

$$\ln(-\ln(1 - X_{drx})) = \ln k + n \ln \frac{\varepsilon - \varepsilon_c}{\varepsilon_p}, \qquad \varepsilon_c \le \varepsilon \le \varepsilon_{ss}. \tag{14}$$

3. **Experimental Results and Discussion**. Function relationship in Eq. (7) was used to conduct fitting calculation of measured stress-strain data. To ensure precision of fitting calculation of $f(\varepsilon)$ function, $g(\varepsilon)$ function was designed as Eq. (15), and a_0, a_1, ..., a_9 as the parameters to be determined. In Fig. 3, taking temperature of 1023 K as examples, the fitting calculated stress was compared to measured stress, indicating that the stress point of fitting calculation was identical to measured stress curve at the temperatures from 773 to 1173 K and strain rates from 0.001 to 1 s^{-1}. It was revealed that $f(\varepsilon)$ function could be used to calculate σ_{rec} and σ_{drx}:

$$g(\varepsilon) = a_0 + a_1 \varepsilon + a_2 \ln \varepsilon + a_3 \varepsilon \ln \varepsilon + a_4 \varepsilon^2 \ln \varepsilon + a_5 \varepsilon (\ln \varepsilon)^2 +$$

$$+ a_6\varepsilon^2 + a_7(\ln\varepsilon)^2 + a_8\varepsilon^3 + a_9(\ln\varepsilon)^3. \qquad (15)$$

Equation (11) was used to calculate the strain hardening rate. Figure 4 shows the curves of strain hardening rate θ and flow stress σ at temperature of 873 K. From point of intersection of $\theta - \sigma$ curve, peak stress and steady state stress can be determined in proper order. Figure 4 shows under strain rate $1\ \text{s}^{-1}$, $\theta - \sigma$ curve is always located above the zero curve because under such deformation conditions there is no obvious dynamic recrystallization in pure copper. Accordingly, the stresses corresponding to the minimum curve values of the peak stress and steady state stress were taken. The same method was used to obtain peak stress and steady state stress at different temperatures and strain rates.
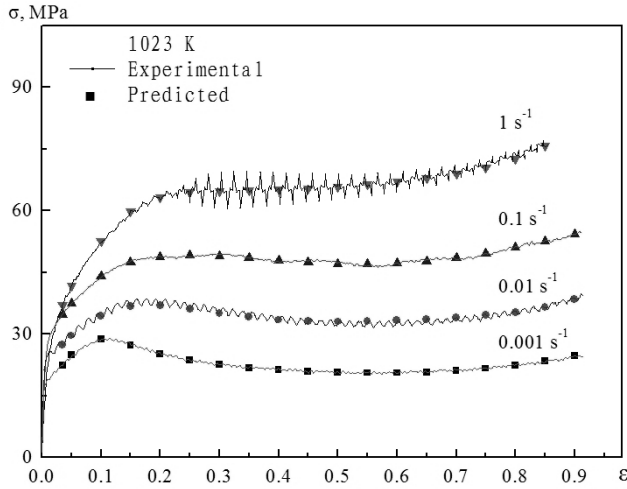

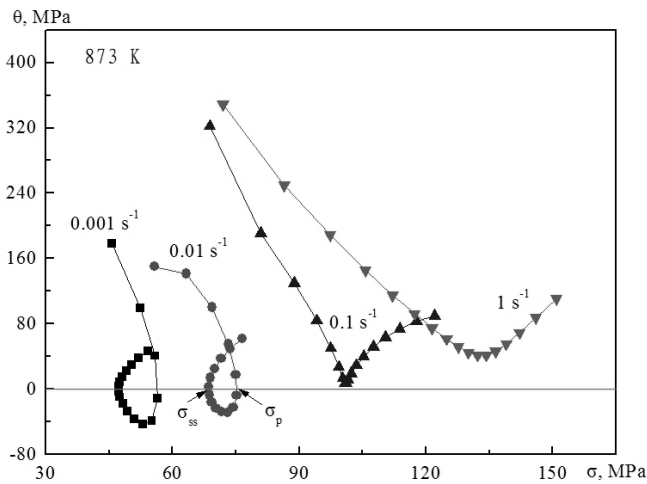Fig. 3. Comparison of predicted flow stresses and the experimental data at $T = 1023$ K.

Fig. 4. Curves of strain hardening rate vs strain at T=873 K.

Within the framework of the proposed method, the peak stress σ_p, steady-state stress σ_{ss}, critical stress σ_c, and saturated stress σ_{sat} were calculated under different
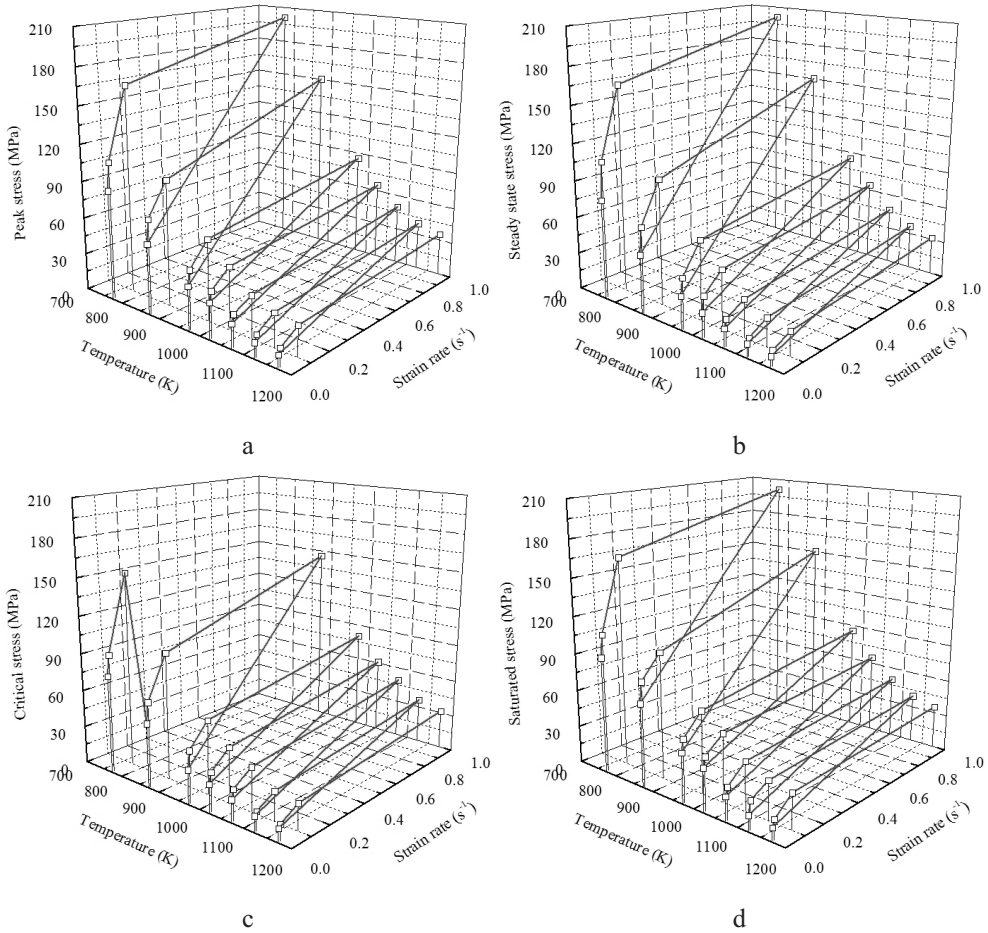
Fig. 5. Temperature and strain rates vs peak stress (a), steady state stress (b), critical stress (c), and saturated stress (d).

temperatures and strain rates, as shown in Fig. 5. Parameters related to Fig. 5 can be used to determine Eqs. (1) and (2). The values of n and k can be obtained by linear regression between $\ln[-\ln(1-X_{drx})]$ and $\ln[(\varepsilon-\varepsilon_c)/\varepsilon_p]$, which is 1.49735 and 0.562980662, respectively.

When $\varepsilon_{ss} \leq \varepsilon \leq 0.9163$, stress increases with the increment of strain, then there occurs the phenomenon of second work hardening. To fit relationship of the second work hardening stress-strain under different temperatures and strain rates, the Johnson–Cook model [14–16], namely Eq. (16), was selected to conduct fitting analysis of stress of the second work hardening. Research results [15] show that the Johnson–Cook model treats the work hardening, strain rate, and thermal effects as independent factors, and does not consider their coupled effect. Moreover, the determination of reference condition is often inappropriate [16]. To avoid these shortcomings, the Johnson–Cook model had been refined in this paper, namely, Eq. (17) was used to conduct fitting calculation of the second work hardening stress–strain data under different temperatures and strain rates:

$$\sigma = (\sigma_{0r} + A\varepsilon_{pl}^B)\left(1+C\ln\frac{\dot{\varepsilon}}{\dot{\varepsilon}_r}\right)\left(1-\left(\frac{T-T_r}{T_m-T}\right)^q\right), \qquad (16)$$

$$\ln \sigma_{wh} = \exp[a_0 + a_1 \varepsilon + a_2 \ln \varepsilon + a_3 \varepsilon \ln \varepsilon + a_4 \varepsilon^2 +$$

$$+ a_5 (\ln \varepsilon)^2] \left(1 + c_0 \left(\ln \frac{\dot{\varepsilon}}{0.001}\right)^{b_0}\right)^{b_1} \left(1 + c_1 \left(\frac{T - 773}{100}\right)^{b_2}\right)^{b_3} \times$$

$$\times \exp\left[\left(1 + c_2 \left(\ln \frac{\dot{\varepsilon}}{0.001}\right)^{b_4}\right)^{b_5} \left(1 + c_3 \left(\frac{T - 773}{100}\right)^{b_6}\right)^{b_7}\right], \quad \varepsilon_{ss} \leq \varepsilon \leq 0.9163. \quad (17)$$

To sum up, Eqs. (1), (2), and (17) take into account the effect of dynamic recovery, dynamic recrystallization, and secondary work hardening on the stress, which make it possible to calculate the stresses under different temperatures and strain rates. The comparison of the experimental data and predictions is depicted in Fig. 2. It can be seen that there is a good agreement between the predicted values and the experimental data.
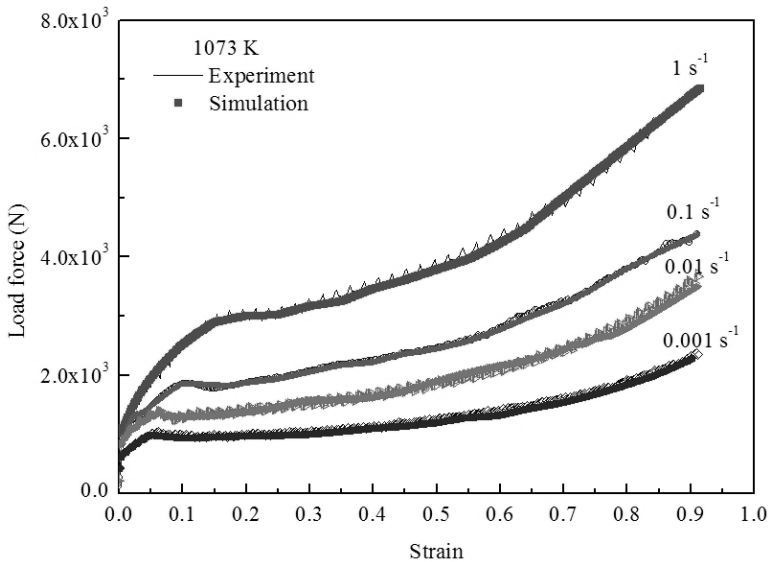

Fig. 6. Variation of load force with strain for pure copper under deformation temperature of 1073 K.

To verify the validity and effectiveness of the developed program, the finite element method (FEM) simulations were performed to analyze upsetting process under different experimental conditions. The billet size of FEM simulations was identical to size of thermal simulation test cylindrical specimens, i.e., diameter of 8 mm and height of 12 mm, the time step of FEM simulations accords with that of the thermal simulation test. Simulation proof of upsetting process was performed. Figure 6 shows the variation of loading force with strain under four different strain rates 0.001, 0.01, 0.1, and 1 s^{-1} at the deformation temperatures of 1073 K. Generally speaking, it illustrates that the loading force simulated by FEM fits in well with the results of compression test. In other words, the simulation results confirm that the developed constitutive equations well describe the flow behavior of pure copper during hot forming process.

Conclusions. The critical conditions for DRX (critical strain and critical stress) are acquired based on the flow stress analysis, and calculation is conducted to obtain saturation stress and parameter *r*; thereby establishing flow stress function of the dynamical recover.

The Avrami's power n and constant k of deformation in the present working conditions are determined as 1.49735 and 0.562980662, respectively. Furthermore, flow stress function of dynamical recrystallization is established. The refined Johnson–Cook model is used in fitting of secondary work hardening stress under different temperatures and strain rates conditions.

A two-dimensional hot upsetting experiment was simulated, it is confirmed that the proposed constitutive equations can be used in numerical simulation in upsetting process of pure copper. It indicates that the developed constitutive equations well describe the flow behavior of pure copper during hot forming process.

1. M. Hörnqvist, N. Mortazavi, M. Halvarsson, et al., "Deformation and texture evolution of OFHC copper during dynamic tensile extrusion," *Acta Mater.*, **89**, 163–180 (2015).

2. W. H. Tian, A. L. Fan, H. Y. Gao, et al., "Comparison of microstructures in electroformed copper liners of shaped charges before and after plastic deformation at different strain rates," *Mater. Sci. Eng. A*, **350**, 160–167 (2003).

3. R. Bobbili, B. V. Ramudu, and V. Madhu, "A physically-based constitutive model for hot deformation of Ti-10-2-3 alloy," *J. Alloy. Compd.*, **696**, 295–303 (2017).

4. X. C. Li, L. L. Duan, J. W. Li, and X. C. Wu, "Experimental study and numerical simulation of dynamic recrystallization behavior of a micro-alloyed plastic mold steel," *Mater. Design*, **66**, 309–320 (2015).

5. C. Zhang, L. W. Zhang, W. F. Shen, et al., "Study on constitutive modeling and processing maps for hot deformation of medium carbon Cr–Ni–Mo alloyed steel," *Mater. Design*, **90**, 804–814 (2016).

6. G. L. Ji, Q. Li, K. Y. Ding, et al., "A physically-based constitutive model for high temperature deformation of Cu-0.36Cr-0.03Zr alloy," *J. Alloy. Compd.*, **648**, 397–407 (2015).

7. M. S. Chen, Y. C. Lin, K. K. Li, et al., "A new method to establish dynamic recrystallization kinetics model of a typical solution-treated Ni-based superalloy," *Comput. Mater. Sci.*, **122**, 150–158 (2016).

8. D. Feng, X. M. Zhang, S. D. Liu, et al., "Constitutive equation and hot deformation behavior of homogenized Al–7.68Zn–2.12Mg–1.98Cu–0.12Zr alloy during compression at elevated temperature," *Mater. Sci. Eng. A*, **608**, 63–72 (2014).

9. R. H. Zhu, Q. Liu, J. F. Li, et al., "Dynamic restoration mechanism and physically based constitutive model of 2050 Al-Li alloy during hot compression," *J. Alloy. Compd.*, **650**, 75–85 (2015).

10. H. Matsumoto and V. Velay, "Mesoscale modeling of dynamic recrystallization behavior, grain size evolution, dislocation density, processing map characteristic, and room temperature strength of Ti-6Al-4V alloy forged in the ($\alpha + \beta$) region," *J. Alloy. Compd.*, **708**, 404–413 (2017).

11. I. Mejia, F. Reyes-Calderon, and J. M. Cabrera, "Modeling the hot flow behavior of a Fe–22Mn–0.41C–1.6Al–1.4Si TWIP steel microalloyed with Ti, V and Nb," *Mater. Sci. Eng. A*, **644**, 374–385 (2015).

12. N. Haghdadi, D. Martin, and P. Hodgson, "Physically-based constitutive modelling of hot deformation behavior in a LDX 2101 duplex stainless steel," *Mater. Design*, **106**, 420–427 (2016).

13. K. Tan, J. Li, Z. J. Guan, et al., "The identification of dynamic recrystallization and constitutive modeling during hot deformation of Ti55511 titanium alloy," *Mater. Design*, **84**, 204–211 (2015).

14. T. Mirzaie, H. Mirzadeh, and J. M. Cabrera, "A simple Zerilli–Armstrong constitutive equation for modeling and prediction of hot deformation flow stress of steels," *Mech. Mater.*, **94**, 38–45 (2016).

15. H. Mirzadeh, "Constitutive modeling and prediction of hot deformation flow stress under dynamic recrystallization conditions," *Mech. Mater.*, **85**, 66–79 (2015).

16. G. B. Wei, X. D. Peng, A. Hadadzadeh, et al., "Constitutive modeling of Mg–9Li–3Al–2Sr–2Y at elevated temperatures," *Mech. Mater.*, **89**, 241–253 (2015).